Nano Energy 52 (2018) 381–390

Contents lists available at ScienceDirect

Nano Energy

journal homepage: www.elsevier.com/locate/nanoen

Communication

Imaging of 3D morphological evolution of nanoporous silicon anode in lithium ion battery by X-ray nano-tomography

Chonghang Zhao[a], Takeshi Wada[b], Vincent De Andrade[c], Doğa Gürsoy[c,d], Hidemi Kato[b], Yu-chen Karen Chen-Wiegart[a,e,*]

[a] Department of Materials Science and Chemical Engineering, Stony Brook University, Stony Brook, NY 11794, United States
[b] Institute for Materials Research, Tohoku University, Katahira, Sendai 980-8577, Japan
[c] Advanced Photon Source, Argonne National Laboratory, Argonne, IL 60439, United States
[d] Department of Electrical Engineering & Computer Science, Northwestern University, Evanston, IL 60208, United States
[e] National Synchrotron Light Source II, Brookhaven National Laboratory, Upton, NY 11973, United States

ARTICLE INFO

Keywords:
Nano-CT
TXM
Nanofoam
LIB
Failure mechanism

ABSTRACT

Nanostructured silicon with its high theoretical capacity and ability to accommodate volume expansion has attracted great attention as a promising anode material for Lithium ion (Li-ion) batteries. Liquid metal dealloying method, is a novel method to create nanoporous silicon (np-Si). The assembled Li-ion batteries based on such np-Si anode can be cycled beyond 1500 cycles, in 1000 mA h/g constant capacity cycling mode with consistent performance; however, it suffers from degradation after ~ 460 cycles, while being cycled under 2000 mA h/g. To reveal the failure mechanism and differences in the morphological evolution in different capacity cycling modes in the np-Si anode, we conducted synchrotron X-ray nano-tomography studies. The three dimensional (3D) morphological evolution was visualized and quantified as a function of the number of cycles and cycling capacities. By comparing the 3D morphology under each cycling condition and correlating these 3D morphological changes with cycling-life performance, we elucidate the failure mechanism of the np-Si electrodes resulting from a mesoscopic to macroscopic deformation, involving volume expansion and gradual delamination. In particular, the shorter cycling life in higher-capacity cycling mode stems from particle agglomeration. Overall, while the nanoporous structure can accommodate the volume expansion locally, these mesoscopic and macroscopic deformations ultimately result in heterogeneous stress distribution with faster delamination. The work thus sheds the light on the importance to consider the structural evolution at the mesoscopic and macroscopic scales, while designing nano-structured energy storage materials for enhanced performances, particularly for long cycling-life durability.

1. Introduction

Silicon (Si) with its high theoretical capacity of 3578 mA h/g, in comparison of 372 mA h/g for carbon-based electrodes, and relative low discharge potential, has attracted attentions as a promising anode material for Li-ion batteries [1]. However, Si electrodes experience a ~ 300% of volume expansion during lithiation, followed by large volume shrinkage during de-lithiation [1]. This drastic morphological change can lead to pulverization of electrode and degradation of battery performance [2]. To prevent or accommodate the extreme volume changes, different methods have been developed, where designing Si anode nano-structure is one of the most promising routes. Different Si nano-structures including nano-tubes [3], nanowires [4], nanoporous Si [5,6], Si hollow particles [7] and Si-C composite [8,9] have been developed to mitigate the structural degradation of Si anode during the cycling of the batteries. Among these nano-structures, nanoporous Si with its properties, including interconnected pores for materials transportation and volume buffering, large surface area for rapid lithiation and delithiation, has become a promising candidate to be used as a Si anode in Li-ion batteries [10,11]. To fabricate nanoporous silicon (np-Si), disproportionation reaction of SiO [10], etching Si with hydrofluoric acid based solution [6] and etching dual phase alloys [12] have been conducted with the resulting electrodes showing promising battery cycling performances.

As an alternative route to design and fabricate np-Si, recently Wada et al. applied a liquid metal dealloying (LMD) method, also known as

* Corresponding author.
E-mail address: Karen.Chen-Wiegart@stonybrook.edu (Y.-c.K. Chen-Wiegart).

https://doi.org/10.1016/j.nanoen.2018.08.009
Received 4 June 2018; Received in revised form 24 July 2018; Accepted 6 August 2018
Available online 08 August 2018

the metallic melt dealloying method, to fabricate interconnected np-Si [5]. Mg_2Si powders were dealloyed in Bi metallic melt to create a bi-continuous structure of Si/Bi-Mg via dynamically rearranging the Si morphology during dealloying of Mg_2Si. This phase separation process is then followed by nitric acid etching of the Bi-Mg phase to create the np-Si particles. The resulting np-Si has a porosity of 60.4%, which can in theory accommodate volume expansion to 253%, corresponding to a ~ 2000 mA h/g capacity. This is based on a linear relation between capacity and volume changes [13]. The Li-ion batteries with anode fabricated from np-Si showed a long cycling life for more than 1500 cycles without degradation under 1000 mA h/g constant capacity condition. However, when cycled under the 2000 mA h/g constant capacity condition, the batteries failed after few hundred cycles [5]. The underlying mechanism responsible for this mismatch between the theoretical prediction and experimental results regarding the battery cycling life is unresolved [5]. The failure mechanism of the Li-ion batteries with np-Si electrodes fabricated by this new LMD method, in particular as a function of cycling capacity, thus requires further investigation and motivated this work.

Microscopic studies have revealed a degradation mechanism of individual nano- or micron-size Si particles/nanowires in Li-ion batteries [14–16]. The crystallography-dependent anisotropic lithiation and heterogeneous volume expansion were attributed to capacity fade of the Si anode [17]. The preferential expansion along $< 110 >$ of crystalline Si anodes, controlled by movement of interfaces was experimentally confirmed in Si nanopillars [18], micropillars [19] and micron-size Si bar using SEM [18–20]. 3D characterization using lab-based X-ray micro-tomography has been performed to investigate the cracking of individual micron-structured Si anode [14,21]. The condition of crack nucleation and initiation from surface of Si nanoparticles were also studied by experiments and simulation [22,23]. To prevent fracture, a critical non-fractured diameter was determined, as 150 nm for crystal Si particle, 300 nm for Si nanowires and 870 nm for amorphous nanoporous Si [23–25].

In addition to individual particles' cracks and mechanical failure, additional factors concerning the overall morphological evolution of the electrode may also contribute to the Si anodes' failure. The morphological evolution of Si electrodes with structure size from hundreds of nanometer to micrometer structure size has also been studied beyond single-particle view [21,26–28]. Radvanyi et al. [29] studied porosity and pore size distribution, and attributed the failure of anodes with Si nanoparticles to limiting Li ion diffusion. Similarly, the non-uniform polarization developed during the cycling of micron Si particles has also been characterized by Li et al. [30], and they attributed the failure to an electrode layer rupture, which leads to conductive network break. The preferential lithiation direction and delamination leading to the failure of electrode with Si micropillar were also confirmed by Shi et al. [19]. The morphological studies were also combined with mechanical measurement and computational modeling to explore the morphological failure among the electrode [17,19,29,30]. The correlation between mechanical stability and structural aspect ratio was studied by Aifantis et al. [31]. These studies of Si electrode shed a light on the importance to analyze the Si electrode from mesoscopic to macroscopic length scale. Understanding the np-Si morphological evolution leading to the failure thus requires not only a high spatial resolution to visualize the np-Si particles, but also a larger imaging field of view to simultaneously resolve the overall morphological evolution in the electrode.

To visualize batteries' complex morphological evolution, recently 3D characterization by X-ray ptychographic tomography [32], transmission X-ray microscopy (TXM) and focus ion beam/scanning electron microscopy (FIB-SEM) [26] have gained attention in analyzing battery materials. These 3D imaging techniques enable observation of 3D morphological changes at sub-50 nm resolution with tens of microns field of view, and thereby provide further detailed 3D morphological information over a representative volume. TXM, with its ability of studying battery cycling in situ, identifying phases based on X-ray attenuation as well as quantifying 3D geometric factors including feature size, shape, tortuosity and curvatures, has been applied to study different batteries and electrodes [14,33–41]. Furthermore, as there is an interest in combining X-ray imaging techniques with other X-ray techniques as a multi-modal approach [42–44], TXM can be combined with other techniques, including spectroscopy [41,45] and X-ray diffraction [46,47] for complementary analysis. Combined with computational techniques such as Digital Volume Correlation or simulation, volumetric strain evolution in electrodes can also be analyzed [27,48].

The goal of this work is to study this unexpected faster failure of Li-ion batteries with np-Si anode fabricated by LMD, emphasizing on the 3D morphological evolution under different cycling-capacity conditions to clarify the failure mechanism. Our work complements prior important 3D imaging work in the field, including 3D microscopic studies conducted on initial cycling of Si particles focusing on single or few particles [14,21] and works conducted by X-ray tomography on overall micron- size Si electrodes [27,28,36,47]. Here, we used synchrotron X-ray nano-tomography to characterize np-Si electrodes with long-term cycling at a sub-60 nm spatial resolution with a 50–60 μm field of view to study a representative volume of Si electrodes with nano-scale features. The 3D morphological evolution of the np-Si electrodes was visualized via nano-tomography using TXM and quantified via 3D image analysis at different stages to elucidate the failure mechanism, especially the influential of cycling capacity condition. This sheds the light on studying and applying nano-size alloy materials as energy storage materials.

2. Experiments

2.1. Nanoporous Si fabrication and battery cells preparation

Np-Si powders (Fig. 1A) were prepared following the previously published experimental procedure [5]. The np-Si powders were rinsed by deionized water and dried in oven at 373 K for an hour. The single crystal np-Si powder with average 400 nm diameter pore size, up to 300 nm facet single crystal size and 60.4 vol% porosity was obtained. To prepare the electrode slurry, the np-Si powders were mixed with acetylene black and polyimide precursor by weight ratio of 60:25:15. The slurry was coated on Cu current collectors and dried for 4 h under 723 K in vacuum. The resulting electrode was then punched into disk and assembled into coin cell (2032), with polytetrafluoroethylene as separator, lithium foil as counter electrode, and 1 mol/l $LiPF_6$ in fluoroethylene carbonate as electrolyte.

2.2. Electrochemical cycling of nanoporous Si battery cells

To study and compare the failure mechanism under fully lithiated and partially lithiated conditions, batteries were cycled in constant charging capacity mode, with 1000 mA h/g and 2000 mA h/g capacity respectively. As this work emphasized on the long-term morphological evolution and degradation after hundreds or even over 1500 cycles, separate samples need to be prepared and examined during the synchrotron X-ray beamtime. The voltage window used during the electrochemical cycling was 0.0–1.0 V vs. Li/Li^+. For the initial 10 cycles, the cycling current was set to 0.5 C, and it increased to 1 C after the initial 10 cycles. The lower current at the initial cycling was chosen to activate the materials. In addition to the pristine electrode samples, under each cycling capacity condition (1000 mA h/g and 2000 mA h/g), three samples with different number of cycles were prepared for characterization, including one at the initial cycle stage, one in the mid-cycling stage without capacity loss, and one close to failure, where significant capacity loss was observed. The cell cycled under the 1000 mA h/g condition, was first lithiated to 1570 mA h/g, followed by a de-lithiation process. It was then lithiated under 1000 mA h/g, after which the tomographic data was measured. Therefore, in the sample group under constant 1000 mA h/g cycling capacity, cycled samples

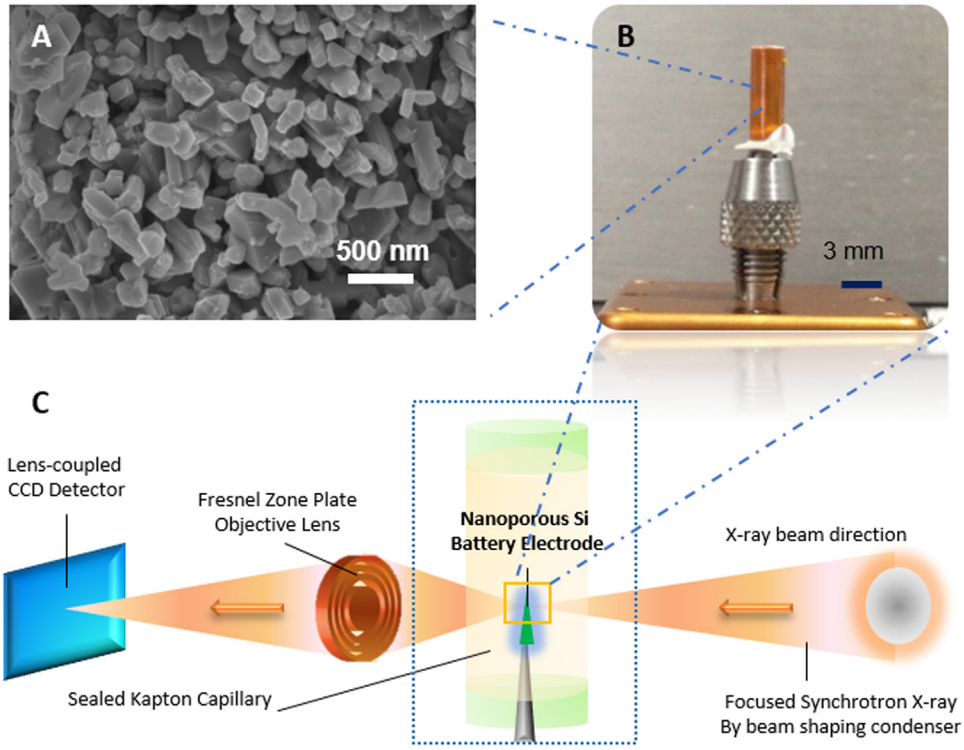

Fig. 1. Sample preparation and experimental setup. (A) The SEM image of as-prepared np-Si, (B) Enclosed np-Si anode for X-ray nano-tomography. (C) Experimental setup for X-ray nano-tomography at the Transmission X-ray Microscopy beamline 32-ID-C, Advanced Photon Source, Argonne National Laboratory. The blue dashed-line rectangle indicates the enclosed np-Si anode as shown in (B). The orange rectangle indicates the X-ray field of view. The illustration is not drawn to scale.

with 2nd lithiation, 500 cycles and 1556 cycles were selected. In the other sample group under 2000 mA h/g cycling capacity condition, cycled samples with 1st lithiation, 100 cycles, and 460 cycles were selected.

2.3. Sample preparation for X-ray nano-tomography characterization

To prepare samples for X-ray nano-tomography characterization, cycled batteries were carefully opened in an Ar-filled glove box located at the Advanced Photon Source (APS), Argonne National Laboratory (ANL). The anode electrodes, including the current collector, were cut and mounted onto the sample mounting pin. To be compatible with the field of view of the Transmission X-ray Microscopy and to ensure sufficient X-ray transmission, the tip of the electrode sample was controlled to be less than 50 μm in diameter. Each of the cut electrode was sealed in a Kapton capillary by Torr seal epoxy in the glove box to prevent the electrode from exposure to the air (Fig. 1B). The samples were kept in the glove box and only transferred to the beamline right before the measurements.

2.4. Synchrotron X-ray microscopy characterization

The X-ray nano-tomography characterization was conducted at the Transmission X-ray Microscopy (TXM) beamline 32-ID-C, APS, ANL [49]. A beam shaping condenser [50] was used to illuminate the sample. A Fresnel zone plate with 60 nm outmost zone width was used as an objective lens. Monochromatic beam with energy at 7.11 ~ 8 keV was used and the measurements were conducted with absorption contrast mode. A lens-coupled optical objective lens with 5× magnification was used with a field of view of 52 × 62 μm^2 (Fig. 1C). For each sample with specific cycling condition, 1201 projections were collected in 180° angular range, corresponding to an angular step size of 0.15°, and saved in Scientific Data Exchange format [51].

To reconstruct the internal 3D structure from the X-ray nano-tomography measurement data, a filtered-backprojection (FBP) algorithm was applied. The weights of the FBP algorithm were selected as to mimic the simultaneous iterative reconstruction technique (SIRT) algorithm based on an optimization procedure [49]. As the tomographic reconstruction software, we used, TomoPy [52], which is a Python package that was initially developed at the APS, and now is an open-source community-driven project. The SIRT-FPB implementation for Graphical-Processing Units (GPUs) was used, which is available in the ASTRA plug-in of TomoPy [53]. The ring removal algorithm was applied in the image processing [54]. 3D morphological parameters were analyzed based on 3D reconstructed images. 2D smoothing and thresholding segmentation were applied to each image slice in freeware Image J. Visual comparison of morphological evolution was conducted in commercial software Avizo (v.9.0 FEI). Customized Matlab codes for morphology analysis, including thickness analysis and density evolution, were developed in-house by the authors at Stony Brook University and Brookhaven National Laboratory.

3. Results and discussions

3.1. Li-ion battery performance with nanoporous Si anode

The np-Si with ~ 60.4% porosity can accommodate a volume expansion as high as 253%, corresponding to lithiation capacity of 2000 mA h/g; this is based on a calculation that the lithiation capacity is approximately linear to volume expansion [13], Therefore, the np-Si battery cells were cycled galvanostatically under the conditions of 1000 mA h/g and 2000 mA h/g in constant charge capacity mode. Fig. 2A shows voltage-capacity curves of Li-ion batteries with np-Si anodes after 2nd lithiation, 100, 500, and 1556 cycles in 1000 mA h/g constant capacity mode. The voltage-capacity curves of the np-Si batteries after 500 and 1556 cycles are similar and both show good performance without much capacity loss. The electrochemical data shows that the nanoporous structure is able to accommodate volume expansion of the Si anodes and thereby ensures the batteries' cycling durability.

Voltage-capacity curves of np-Si batteries cycled in 2000 mA h/g constant capacity mode, after 1st lithiation, 10, 100 and 460 cycles are shown in Fig. 2B. The significant polarization during the first cycle indicates that the active materials did not fully react with Li ions;

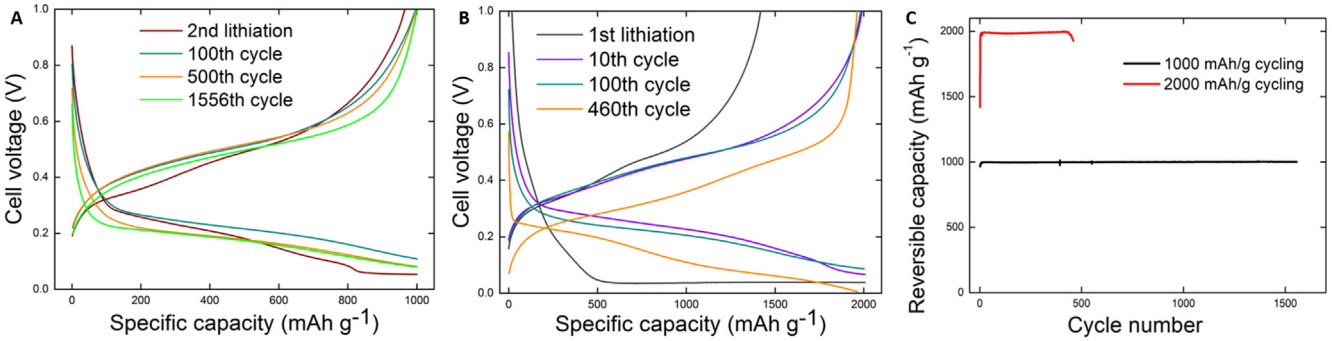

Fig. 2. Battery performance with nanoporous Si anode. (A) voltage-capacity curve of battery cycled in 1000 mA h/g constant capacity mode. Initial 10 cycle rate was 0.5 C, and later cycles were 1 C. (B) voltage-capacity curve of battery after 1st lithiation, 10, 100, 460 cycles in 2000 mA h/g constant charge capacity mode. After Initial 10 cycle at 0.5 C rate, rate was controlled at 1 C. (C) Reversible capacity vs. cycle numbers for both 1000 mA h/g and 2000 mA h/g constant capacity cycling modes.

potentially only the outer portion of np-Si in the electrode participated in the reaction. After 435th cycle, the batteries began to degrade, and its reversible capacity can no longer reach 2000 mA h/g. Moreover, the decreased potentials for both the charging and discharging potential plateaus indicate that cell polarization reduces potential, which attributes to structural failure. For both cycling conditions, 1000 mA h/g and 2000 mA h/g, the reversible capacity of the electrodes *vs*. cycle number are shown in the Fig. 2C. As expected, nanoporous structure can accommodate volume expansion at 1000 mA h/g and the np-Si cell can be electrochemically cycled over 1556 cycles without capacity loss. However, under the 2000 mA h/g cycling condition, battery began to degrade after 435 cycles.

3.2. 3D Morphological evolution of nanoporous Si electrode

The 3D X-ray nano-tomography results of pristine np-Si electrodes and np-Si cycled in 1000 and 2000 mA h/g constant cycling capacity modes are shown in Fig. 3 with 3D volume rendering. In the pristine sample, Si particles are distributed relatively homegeneously on the current collector. The average thickness of pristine samples is 2.0 ± 0.5 μm, which also indicates the standard deviation of the thickness.

3.2.1. Morphological evolution in lower cycling capacity (1000 mA h/g)

Fig. 3B shows the morphological evolution of electrodes cycled under constant 1000 mA h/g capacity. After the 2nd lithiation, the overall thickness of electrode increased and the np-Si particles in the electrode shifted away from the current collector. As no capacity changes at this state, the electrode is believed to largely remain in contact with the current collector without significant delamination, despite the large volume changes. The materials between the np-Si particle clusters and the current collector are the light element phases such as carbon and pores, which exhibit less attenuation in the X-ray microscopy as later shown in the pseudo cross-section in the Fig. 4A. These light element phases can be found throughout the samples, and can also be visualized at the surface of the samples in back-scattering SEM images (Supporting information Fig. S2 and Fig. S3). Partial delamination is possible which will be discussed in the next section. Quantitative analysis of the thickness evolution, as shown in Fig. 3D, shows that a relative thickness expansion of 100% occurred after the 2nd lithiation with the constant capacity cycling of 1000 mA h/g. Note that aside from Si particles, the average electrode thickness also include other non-active materials, such as carbon black as conductive materials and polyimide as binder. The thickness analysis measures the height from the surface of electrode to the top of the current collector. Therefore, the macroscopic structural changes such as swelling and development of pores will also contribute to the overall thickness changes.

After 500 cycles, the electrode expanded more than eight times of the pristine one. This greater volume expansion than the theoretical Si volume expansion is due to the development of the macroporous structure. The large error bar in Fig. 3D represents the standard deviation and thus reflects the heterogeneous structure of electrode. However, it needs to be emphasized that the 3D structure of electrode (Fig. 3B) shows that the entire electrode structure remained well-connected at this stage, and the partial delamination from current collector did not lead to active materials loss. As a result, the battery performance did not degrade after 500 cycles under the 1000 mA h/g condition. Note that under the lower capacity cycling condition, even if the np-Si electrode loses 2/3 of active materials, the battery's theoretical capacity may still reach 1000 mA h/g.

Finally after 1556 cycles, the average thickness of the electrode decreased significantly and a larger amount of electrode delaminated from current collector, which is shown in Fig. 3B. However, this observation may only represent a local phenomenon within the tens of micron field of view; as indicated in the electrochemical cycling data, the entire electrode did not delaminate from current collector – a large part of electrode still remained attached, and continued to support the electrochemical reactions.

3.2.2. Morphological evolution in higher cycling capacity (2000 mA h/g)

The 3D morphological evolution of np-Si electrode cycled under 2000 mA h/g is shown in Fig. 3C. After the first lithiation, the morphology of the electrode evolved more significantly than the electrode cycled under 1000 mA h/g after the 2nd lithiation. Much larger particles/agglomeration can be found in the cycled electrode and lead to a significant thickness variation, which corresponds to the larger error bar in the average thickness analysis. The average thickness of the electrode expanded more than 200% (Fig. 3E) from the pristine sample, which is higher than the theoretical calculation if only the np-Si expands. This indicates that after the first half cycle, the higher cycling capacity of 2000 mA h/g leads to an overall larger macroscopic expansion, including the non-active phases. After 100 cycles, small agglomeration and partially lithiated np-Si can still be found in the electrode. The electrode became thinner than a sample taken after 1st lithiation, indicating a delamination process which leads to active materials loss. After 460 cycles, the battery lost most of its active materials, with thin residual electrode remaining on the current collector. This significant difference results in fast degradation right after 435 cycles under 2000 mA h/g cycling condition.

3.3. 3D Material density evolution is due to electrochemical lithiation/delithiation

Normalized X-ray attenuation maps in Fig. 4 show the materials density evolution in the np-Si electrode as a function of electrochemical

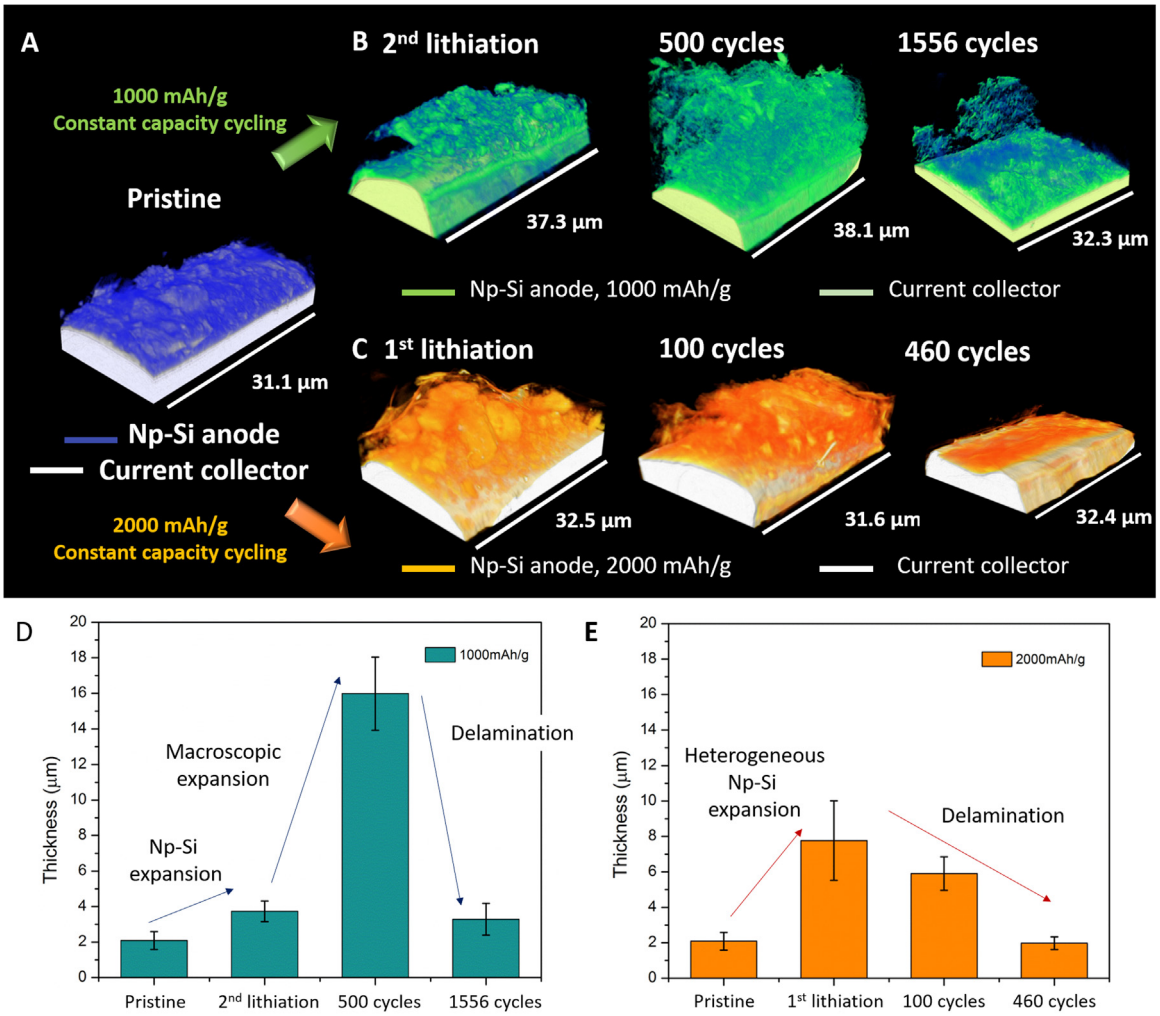

Fig. 3. X-ray nano-tomography reconstruction with volume rendering shows the morphological evolution of the np-Si anode (A) Pristine np-Si electrode (B) Under 1000 mA h/g constant capacity cycling: pristine electrode, electrode galvanostatically cycled after the 2nd lithiation, 500 cycles and 1556 cycles. (C) Under 2000 mA h/g constant capacity cycling: after the 1st lithiation, 100 cycles and 460 cycles. (D–E) Quantitative analysis of thickness evolution in the Si anode for different constant-capacity cycling modes: (D) 1000 mA h/g, and (E) 2000 mA h/g.

cycling times under the constant capacity condition 1000 mA h/g. The normalized colorscale directly corresponds to the X-ray attenuation, and thus directly represents the density of the materials in 3D. For instance, the lower X-ray attenuation, represented in blue, corresponds to the lower material density and hence a lithiated phase – there is a higher volumetric fraction of Li per unit Si; while the higher X-ray attenuation, represented in red, corresponds to the higher material density and hence a delithiated phase, lower volumetric fraction of Li per unit Si. For visualization purpose, the color of current collectors is set to gray.

3.3.1. *Material density evolution in lower capacity cycling (1000 mA h/g)*

In 1000 mA h/g cycling, after the 2nd lithiation, the material density decreased, which was reflected on the overall lower X-ray absorption coefficient of the materials. The np-Si particles' movement away from the current collector after the 2nd lithiation, as also shown in Fig. 3, can be observed quantitatively here: The more-lithiated np-Si particles (red circled in Fig. 4A, less density, less X-ray attenuated) delaminated further away from the current collector, while less-lithiated np-Si particles (yellow circled in Fig. 4A, higher density, higher X-ray attenuated) remained more attached to the current collector. It can be understood as the more-lithiated part of the electrode experienced volume expansion and applied more stress to the electrode and current collector, leading more delamination from current collector.

This behavior was quantified as normalized X-ray attenuation vs. distance to the current collector, as shown in Fig. 4C. Overall, it shows a decrease of normalized gray scale from left to right, indicating distribution of X-ray attenuation coefficient from highly X-ray absorbed copper current collector to the lower absorbed Si and carbon. In the pristine sample, the small plateau represents relative condense and uniform pristine np-Si electrode, corresponding to normalized gray scale as 0.2. After the 2nd lithiation, the normalized X-ray attenuation dropped significantly to 0.07, which is shown by the gray curve. The variation in the X-ray attenuation as a function of the distance from the current collector indicates a non-uniform lithiation and volume expansion process during charging. After 500 cycles, the electrode pulverized and partially delaminated from current collector; significant macroscopic morphological changes continued, as shown in Fig. 4A; the X-ray attenuation as the function of distance also varied more significantly after 500 cycles, as shown in Fig. 4C.

The overall structure after 1556 cycles under 1000 mA h/g cycling condition showed a significant delamination. Despite that, part of the structure remained connected and the region close to the current collector showed a larger X-ray attenuation, which is different from other samples. There are two possible explanations for this phenomenon: (1) The surface of current collector was rough, and the gray scale

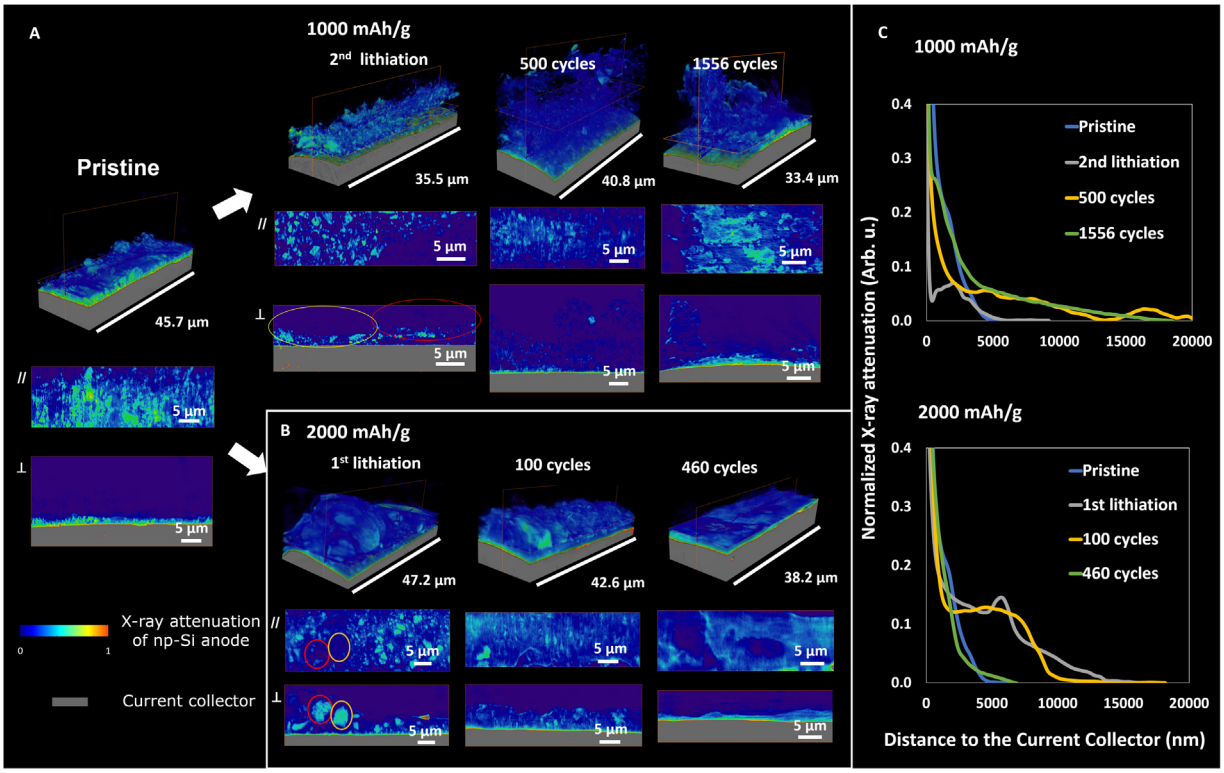

Fig. 4. Quantitative material density 3D maps and pseudo cross-sections from X-ray nano-tomography showing electrode cycled in constant capacity mode (A) 1000 mA h/g, and (B) 2000 mA h/g. In the pseudo cross-sections parallel (noted as '//') to the current collector, a fixed distance of 972 nm from the shown plane to the top of current collector is chosen for all the reaction conditions. The pseudo cross-sections perpendicular to the current collector are also shown here, noted as '⊥'. (C) Normalized X-ray attenuation as a function of the distance to the current collector. The X-ray attenuation is normalized to 1.0 for the current collector and to 0.0 for the air.

represents a mixture of current collector and electrode, which led to a higher gray scale at the interface. This explanation is consistent with Kataoka et al.'s finding that a current collector may deform when the deposited electrode experiences significant volume expansion; such deformation of the current collector can also reduce electrical conductivity and lead to limited utilization of active materials [55]. (2) Li ion diffusion within the electrode was heterogeneous. The lithiated and expanded Si structure hindered the Li ion diffusion path within the electrode, leaving less-lithiated np-Si particles at the bottom of the electrodes. Moreover, as the lithiated region experienced more stress from the lithiation-induced volume expansion, it tends to delaminate from the rest of the electrode. Here, sample-to-sample variation and heterogeneity within a sample may affect the quantification from the sampled volume. Therefore, *ex situ* or in situ characterization on the same sample will be important for future studies.

3.3.2. *Material density evolution in higher capacity cycling (2000 mA h/g)*

For the np-Si electrode cycled under higher constant capacity, 2000 mA h/g, the structure underwent a much more heterogeneous evolution than in the lower constant capacity cycling case. After the 1st lithiation, the X-ray attenuation also decreased, as in the lower cycling capacity case. Interestingly, the X-ray attenuation of the electrode after initial cycling, which represents the material density, remained higher in average under the 2000 mA h/g condition than the one under the 1000 mA h/g cycling condition, although locally some parts have evolved into a less-attenuated lithiated phase. Moreover, the material density distributed more heterogeneously within the electrode. This indicates an agglomeration process, associated with heterogeneous lithiation process that limits utilization of active materials.

The peak in X-ray attenuation distribution corresponds to the large partially lithiated Si mixture within the electrode, which is also indicated by the circles in the pseudo cross-section in Fig. 4B. In the red-circled region, the lithiated, then agglomerated Si can be clearly found, and its less X-ray attenuation compared to the pristine sample confirms the lithiation process. In the orange-circled region, X-ray attenuation is higher in the center than the boundary region, and more condensed than the red-circled region. It is likely that this was an agglomerated pristine Si, and then limited lithiation process occurred at the boundary. This result is consistent with Luo et al.'s study [56].

In addition, the Si distribution is not homogeneous among the current collector. At the bottom of the red-/orange-circled regions, where large np-Si agglomeration existed, few separated np-Si particles can be found near the current collector; other regions, on the other hand, have relatively homogeneously distributed np-Si particles. This confirmed the movement and agglomeration of np-Si particles during the higher capacity cycling. The agglomeration has been explained as an electrochemical sintering process between nano-size particles, which happens during volume expansion [29,56,57]. Under the higher cycling capacity condition (2000 mA h/g), the expanded Si ligaments occupied more porous space, so that np-Si particles agglomerated together more easily. On the contrary, under the lower cycling capacity condition (1000 mA h/g), the porous structure could accommodate the most volume expansion during lithiation, and the agglomeration during lithiation was alleviated.

After 100 cycles under 2000 mA h/g cycling condition, small agglomeration and partially lithiated Si particles can still be found within the electrode and the region close to the current collector. The X-ray attenuation distribution vs. the distance to the current collector became more homogeneous. However, the X-ray attenuation value was still higher than the electrodes cycled under 1000 mA h/g condition. This can be attributed to the mixture of more pristine and partially lithiated Si within the electrode. This is also consistent with the visualization based on pseudo cross-sections (Fig. 4). It is likely that the larger volume expansion under 2000 mA h/g condition leads to a higher degree

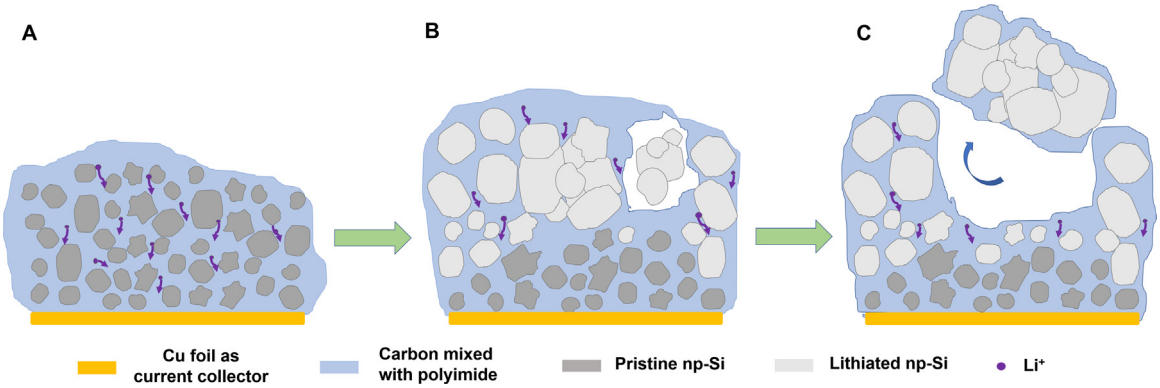

Fig. 5. Schematics of the capacity failure mechanisms in np-Si under higher capacity cycling, caused by agglomeration occurred during the early cycles. (A) Pristine electrode at initial cycling condition, (B) agglomeration separates the active materials from conductive network, leading to a local fading mode of failure mechanism; agglomeration also inhibits the Li^+ diffusion path, and (C) finally the agglomeration leads to delamination and active materials loss.

of particle disconnection from the conductivity network; as a result, more active materials cannot involve in the electrochemical reaction. Finally, after 460 cycles, the battery lost most of its active materials, with thin residual layer of electrode remaining on the current collector. This morphology is different from result in 1000 mA h/g group and can explain the fast degradation right after 435 cycles.

3.4. Failure phenomenon and mechanisms

3.4.1. Pulverization of np-Si

At the later stage of the electrochemical cycling, Si particles can hardly be identified from other materials in the electrode in both the pseudo cross-sections and the 3D volume rendering. This disappearance of well-defined Si particles happened in both the 1000 mA h/g (after 500 cycles) and 2000 mA h/g (after 100 cycles) conditions.

It is likely that the np-Si particles were pulverized to the size that is lower than the image resolution and cannot be distinguished from each other. This phenomenon is also consistent with Etiemble et al.'s finding – they found that after 100 cycles, the Si particles pulverized to the size lower than the SEM resolution [26]. The interaction between different lithiated ligaments during volume expansion may not be the only cause for pulverization; the compressive and tensile stresses generated from phase transformation process during charging and discharging can also lead to stress evolution and fracture [17]. The phase transformation from crystal Si to lithiated amorphous Si can occur in such nanoporous crystal Si structure. This explains why even though there are sufficient porous space between Si ligaments, the np-Si still pulverized. To alleviate the fracture, determining the critical size for the np-Si structure and controlling the ligament size lower than such critical size will be helpful, and can be achieved by controlling the dealloying processing parameters, such as precursor composition, dealloying time and temperature [45,58]. Moreover, on each ligament, finer porous structure can also be formed by diffusion of Si atoms [59]. However, we should emphasize that the pulverization of np-Si particle did not lead to a significant capacity failure. The polyimide as binder materials can bind structure together and keep the pulverized np-Si contact with the conductive network. The strong cross-linked network structure and protected artificial solid electrolyte interface from polyimide both contribute to structural stability and electrical conductivity, maintaining a steady performance, which has been demonstrated in previous polyimide and binder studies [60,61]. Therefore, the battery's capacity did not degrade, even if significant morphological changes occurred.

3.4.2. Partially lithiated np-Si particles and delamination

Partially lithiated Si can be found in the electrode during the cycling, indicated by the heterogeneous X-ray attenuation in Fig. 4. These less fractured, less reacted porous Si powders/ligaments can be explained by a limited Li ion diffusion process, which occurred slower at the distance away from the electrode/electrolyte interface. Prior studies showed that such process can lead to cell failure [29,62]. However, we believe that the limited diffusion only hinders full utilization of the active materials, but is not the main contribution to the cell failure in our particular studied system. Instead, accompanied gradual delamination from electrode surface is the main cause of capacity failure. The potential delamination from current collector is consistent with findings in the work done by Tariq et al. [63], which explained by an inhomogeneous lithiation process within the Si anode. The location-dependent volume expansion leads to local stress and electrode delamination. The heterogeneous volume expansion of Si anode was also found by Zilke et al. [28]. Their characterization results - cracks propagate through electrode thickness – can also be found in our delaminated regions. However, as mentioned, the np-Si particle movement, accompanied by potential partial delamination at limited region, did not lead to battery failure at the beginning and even following electrochemical cycles up to over 1500 cycles under the 1000 mA h/g cycling conditions. Under the 2000 mA h/g cycling condition, the electrode experienced a significant particle agglomeration which also led to a delamination of electrodes; this will be discussed in the following section to highlight the different morphological evolution under higher cycling capacity.

3.4.3. Agglomeration as the key capacity failure mechanism in higher capacity cycling

We would like to emphasize that the agglomeration in 2000 mA h/g cycled cells leads to a faster capacity failure in the np-Si battery cells via three major mechanisms, as illustrated in Fig. 5.

(1) Local fading mode: During lithiation, these agglomerated particles experience larger volume expansion compared to the normal np-Si around. After delithiation, these agglomerations may lose contact with conductive carbon. In this case, initially inserted Li ion will be trapped into Si agglomeration and the agglomerated particles may not be involved in the electrochemical reactions of the following cycles; this leads to a limited utilization of active materials on the anode, as the electrode cannot undergo a full lithiation/delithiation process. This is consistent with Choi et al. 's finding through analyzing Si particles in Li-ion batteries, and they defined this failure mechanism as local fading mode. [64] It is also consistent with our results shown in the pseudo cross-sections: in the partially lithiated Si, agglomeration still exist within the electrode, even after 100 cycles (Fig. 4).
(2) Diffusion path inhibition: The agglomeration of Si particles will block the diffusion path, so that the materials below the agglomerated particles may not be able to react. This explains the residual,

partially lithiated Si near the current collector in the high capacity cycling case. This explanation is consistent with the analysis of failure mechanism conducted by Radvanyi et al. [29].

(3) Stress concentration and delamination: Agglomeration process leads to heterogeneous lithiation process and stress distribution within the electrode. The region near agglomeration is a stress concentration region, which tends to be fractured and more easily detached from the bulk of the electrode. Therefore, when the electrode is delaminated, the crack tends to go through the boundary region of the agglomeration. This results in a loss of active materials. Under the 2000 mA h/g cycling condition, the delamination process is stronger than the one in 1000 mA h/g. Thus, delamination will lose more active materials, and leads to a faster capacity loss. This also explains why the overall electrode thickness is less in 2000 mA h/g after 100 times cycling than the one cycled in 1000 mA h/g after 500 cycles.

4. Conclusion

We conducted 3D X-ray nano-tomography by Transmission X-ray Microscopy and electrochemistry characterization to resolve the morphological evolution of the nanoporous silicon (np-Si) anode electrode during cycling Li-ion batteries. In particular, our results elucidate the effects of higher cycling capacity on the failure mechanism. By comparing the morphological changes under different cycling conditions with lower (1000 mA h/g) and higher (2000 mA h/g) cycling capacities, we can draw conclusions as below:

For both cycling conditions, at the initial cycling stage, np-Si particles were not homogeneously lithiated, which leads to heterogeneous distribution of lithiated np-Si and an overall thickness variation at the macroscopic level. This may result in uneven stress distribution and mechanical instability. The pulverization of np-Si was also observed under both cycling conditions. Such pulverization, however, did not lead to the failure of the batteries.

The key finding for np-Si under different cycling conditions is that the extent of agglomeration differs, which leads to different rates of failure. Under the higher capacity cycling condition, the significant agglomeration caused a heterogeneous stress distribution, limited the utilization of active materials and blocked Li ion diffusion path. Gradual delamination leading to significant loss of active materials from electrodes is the main cause of battery performance degradation. Ultimately the structure fails when the agglomerated structure fully delaminates from the current collector. This was clearly observed in samples cycled under the higher capacity cycling condition (2000 mA h/g) within 500 cycles. The ones cycled under lower capacity cycling condition (1000 mA h/g) showed similar trend at above 1500 cycles; further work is required to fully address the failure mechanism in the lower cycling capacity condition.

To alleviate the delamination in order to extend the cycle life of np-Si anode cells, keeping the structural integrity of electrode at the macroscopic level is crucial. To realize this goal, in addition to designing a nanoporous structure with sufficient porosity and appropriate ligament size below the critical size to accommodate volume expansion, the engineering and designing of the full electrode structure is crucial. The work also demonstrated that the 3D X-ray nano-tomography, combined with visualization and quantitative analysis, is promising to reveal the morphological evolution in energy storage and conversion materials.

Acknowledgements

K. Chen-Wiegart and C. Zhao acknowledge the support of J. Thieme and G. Williams at NSLS-II, and the financial support by the Department of Materials Science and Chemical Engineering, the College of Engineering and Applied Sciences, and the Stony Brook University, as well as by the Brookhaven National Laboratory under Contract No. DE-SC0012704. H. K and T. W. acknowledge the financial support by Creation of Life Innovation Materials for Interdisciplinary and International Researcher Development, Tohoku University. Use of the Advanced Photon Source (APS), a U.S. Department of Energy (DOE) Office of Science User Facility operated for the DOE Office of Science by Argonne National Laboratory under Contract No. DE-AC02-06CH11357. Portions of this work – the use of the Ar-filled glovebox at APS – were performed at the laboratory of HPCAT (Sector 16), Advanced Photon Source, Argonne National Laboratory. HPCAT operations are supported by DOE-NNSA under Award No. DE-NA0001974, with partial instrumentation funding by National Science Foundation. The authors also would like to acknowledge the great support and efforts provided by the HPCAT staff scientists - Curtis Kenney-Benson and Jesse Smith. This research used resources of the National Synchrotron Light Source II, a U.S. Department of Energy (DOE) Office of Science User Facility operated for the DOE Office of Science by Brookhaven National Laboratory under Contract No. DE-SC0012704.

Appendix A. Supplementary material

Supplementary data associated with this article can be found in the online version at doi:10.1016/j.nanoen.2018.08.009.

References

[1] M.N. Obrovac, L.J. Krause, Reversible cycling of crystalline silicon powder, J. Electrochem. Soc. 154 (2007) A103–A108.
[2] W. Wang, M.K. Datta, P.N. Kumta, Silicon-based composite anodes for Li-ion rechargeable batteries, J. Mater. Chem. 17 (2007) 3229–3237.
[3] H. Wu, G. Chan, J.W. Choi, I. Ryu, Y. Yao, M.T. McDowell, S.W. Lee, A. Jackson, Y. Yang, L. Hu, Y. Cui, Stable cycling of double-walled silicon nanotube battery anodes through solid-electrolyte interphase control, Nat. Nanotechnol. 7 (2012) 309–314.
[4] C.K. Chan, H. Peng, G. Liu, K. McIlwrath, X.F. Zhang, R.A. Huggins, Y. Cui, High-performance lithium battery anodes using silicon nanowires, Nat. Nanotechnol. 3 (2008) 31–35.
[5] T. Wada, T. Ichitsubo, K. Yubuta, H. Segawa, H. Yoshida, H. Kato, Bulk-nanoporous-silicon negative electrode with extremely high cyclability for lithium-ion batteries prepared using a top-down process, Nano Lett. 14 (2014) 4505–4510.
[6] M. Ge, Y. Lu, P. Ercius, J. Rong, X. Fang, M. Mecklenburg, C. Zhou, Large-scale fabrication, 3D tomography, and lithium-ion battery application of porous silicon, Nano Lett. 14 (2014) 261–268.
[7] Y. Yao, M.T. McDowell, I. Ryu, H. Wu, N. Liu, L. Hu, W.D. Nix, Y. Cui, Interconnected silicon hollow nanospheres for lithium-ion battery anodes with long cycle life, Nano Lett. 11 (2011) 2949–2954.
[8] Y.Z. Li, K. Yan, H.W. Lee, Z.D. Lu, N. Liu, Y. Cui, Growth of conformal graphene cages on micrometre-sized silicon particles as stable battery anodes, Nat. Energy 1 (2016).
[9] M. Ko, S. Chae, J. Ma, N. Kim, H.W. Lee, Y. Cui, J. Cho, Scalable synthesis of silicon-nanolayer-embedded graphite for high-energy lithium-ion batteries, Nat. Energy 1 (2016).
[10] R. Yi, F. Dai, M.L. Gordin, S. Chen, D. Wang, Micro-sized Si-C composite with interconnected nanoscale building blocks as high-performance anodes for practical application in lithium-ion batteries, Adv. Energy Mater. 3 (2013) 295–300.
[11] X. Li, M. Gu, S. Hu, R. Kennard, P. Yan, X. Chen, C. Wang, M.J. Sailor, J.-G. Zhang, J. Liu, Mesoporous silicon sponge as an anti-pulverization structure for high-performance lithium-ion battery anodes, Nat. Commun. 5 (2014).
[12] Z.Y. Jiang, C.L. Li, S.J. Hao, K. Zhu, P. Zhang, An easy way for preparing high performance porous silicon powder by acid etching Al-Si alloy powder for lithium ion battery, Electrochim. Acta 115 (2014) 393–398.
[13] M.N. Obrovac, L. Christensen, D.B. Le, J.R. Dahnb, Alloy design for lithium-ion battery anodes, J. Electrochem. Soc. 154 (2007) A849–A855.
[14] J. Gonzalez, K. Sun, M. Huang, J. Lambros, S. Dillon, I. Chasiotis, Three dimensional studies of particle failure in silicon based composite electrodes for lithium ion batteries, J. Power Sources 269 (2014) 334–343.
[15] Z.D. Zeng, N.A. Liu, Q.S. Zeng, S.W. Lee, W.L. Mao, Y. Cui, In situ measurement of lithiation-induced stress in silicon nanoparticles using micro-Raman spectroscopy, Nano Energy 22 (2016) 105–110.
[16] L.L. Luo, H. Yang, P.F. Yan, J.J. Travis, Y. Lee, N. Liu, D.M. Piper, S.H. Lee, P. Zhao, S.M. George, J.G. Zhang, Y. Cui, S.L. Zhang, C.M. Ban, C.M. Wang, Surface-coating regulated lithiation kinetics and degradation in silicon nanowires for lithium ion battery, ACS Nano 9 (2015) 5559–5566.
[17] M.T. McDowell, S.W. Lee, W.D. Nix, Y. Cui, 25th anniversary article: understanding the Lithiation of silicon and other alloying anodes for lithium-ion batteries, Adv. Mater. 25 (2013) 4966–4984.
[18] S.W. Lee, M.T. McDowell, J.W. Choi, Y. Cui, Anomalous shape changes of silicon nanopillars by electrochemical lithiation, Nano Lett. 11 (2011) 3034–3039.

[19] F.F. Shi, Z.C. Song, P.N. Ross, G.A. Somorjai, R.O. Ritchie, K. Komvopoulos, Failure mechanisms of single-crystal silicon electrodes in lithium-ion batteries, Nat. Commun. 7 (2016).
[20] J.L. Goldman, B.R. Long, A.A. Gewirth, R.G. Nuzzo, Strain anisotropies and self-limiting capacities in single-crystalline 3D silicon microstructures: models for high energy density lithium-ion battery anodes, Adv. Funct. Mater. 21 (2011) 2412–2422.
[21] O.O. Taiwo, M. Loveridge, S.D. Beattie, D.P. Finegan, R. Bhagat, D.J.L. Brett, P.R. Shearing, Investigation of cycling-induced microstructural degradation in silicon-based electrodes in lithium-ion batteries using X-ray nanotomography, Electrochim. Acta 253 (2017) 85–92.
[22] Y.T. Cheng, M.W. Verbrugge, Diffusion-induced stress, interfacial charge transfer, and criteria for avoiding crack initiation of electrode particles, J. Electrochem. Soc. 157 (2010) A508–A516.
[23] X.H. Liu, L. Zhong, S. Huang, S.X. Mao, T. Zhu, J.Y. Huang, Size-dependent fracture of silicon nanoparticles during lithiation, ACS Nano 6 (2012) 1522–1531.
[24] I. Ryu, J.W. Choi, Y. Cui, W.D. Nix, Size-dependent fracture of Si nanowire battery anodes, J. Mech. Phys. Solids 59 (2011) 1717–1730.
[25] C.F. Shen, M.Y. Ge, L.L. Luo, X. Fang, Y.H. Liu, A.Y. Zhang, J.P. Rong, C.M. Wang, C.W. Zhou, In situ and ex situ TEM study of lithiation behaviours of porous silicon nanostructures, Sci. Rep. 6 (2016).
[26] A. Etiemble, A. Tranchot, T. Douillard, H. Idrissi, E. Maire, L. Roue, Evolution of the 3D microstructure of a Si-based electrode for Li-ion batteries investigated by FIB/SEM tomography, J. Electrochem. Soc. 163 (2016) A1550–A1559.
[27] J. Paz-Garcia, O.O. Taiwo, E. Tudisco, D.P. Finegan, P.R. Shearing, D.J.L. Brett, S.A. Hall, 4D analysis of the microstructural evolution of Si-based electrodes during lithiation: time-lapse X-ray imaging and digital volume correlation, J. Power Sources 320 (2016) 196–203.
[28] L. Zielke, F. Sun, H. Markötter, A. Hilger, R. Moroni, R. Zengerle, S. Thiele, J. Banhart, I. Manke, Synchrotron X-ray tomographic study of a silicon electrode before and after discharge and the effect of cavities on particle fracturing, ChemElectroChem 3 (2016) 1170–1177.
[29] E. Radvanyi, W. Porcher, E. De Vito, A. Montani, S. Franger, S.J.S. Larbi, Failure mechanisms of nano-silicon anodes upon cycling: an electrode porosity evolution model, Phys. Chem. Chem. Phys. 16 (2014) 17142–17153.
[30] T. Li, J.Y. Yang, S.G. Lu, H. Wang, H.Y. Ding, Failure mechanism of bulk silicon anode electrodes for lithium-ion batteries, Rare Met. 32 (2013) 299–304.
[31] K.E. Aifantis, S.A. Hackney, Mechanical stability for nanostructured Sn- and Si-based anodes, J. Power Sources 196 (2011) 2122–2127.
[32] Y.S. Yu, M. Farmand, C. Kim, Y.J. Liu, C.P. Grey, F.C. Strobridge, T. Tyliszczak, R. Celestre, P. Denes, J. Joseph, H. Krishnan, F. Maia, A.L.D. Kilcoyne, S. Marchesini, T.P.C. Leite, T. Warwick, H. Padmore, J. Cabana, D.A. Shapiro, Three-dimensional localization of nanoscale battery reactions using soft X-ray tomography, Nat. Commun. 9 (2018).
[33] M. Ebner, F. Marone, M. Stampanoni, V. Wood, Visualization and quantification of electrochemical and mechanical degradation in Li ion batteries, Science 342 (2013) 716–720.
[34] J. Wang, C. Eng, Y.-cK. Chen-Wiegart, J. Wang, Probing three-dimensional sodiation-desodiation equilibrium in sodium-ion batteries by in situ hard X-ray nanotomography, Nat. Commun. 6 (2015).
[35] J. Wang, Y.-cK. Chen-Wiegart, J. Wang, In operando tracking phase transformation evolution of lithium iron phosphate with hard X-ray microscopy, Nat. Commun. 5 (2014).
[36] F. Sun, H. Markotter, K. Dong, I. Manke, A. Hilger, N. Kardjilov, J. Banhart, Investigation of failure mechanisms in silicon based half cells during the first cycle by micro X-ray tomography and radiography, J. Power Sources 321 (2016) 174–184.
[37] Y.C.K. Chen-Wiegart, P. Shearing, Q.X. Yuan, A. Tkachuk, J. Wang, 3D morphological evolution of Li-ion battery negative electrode LiVO2 during oxidation using X-ray nano-tomography, Electrochem. Commun. 21 (2012) 58–61.
[38] J. Wang, Y.-cK. Chen-Wiegart, J. Wang, In situ three-dimensional synchrotron X-ray nanotomography of the (De) lithiation processes in tin anodes**, Angew. Chem. Int. Ed. 53 (2014) 4460–4464.
[39] Z. Liu, K. Han, Y.C.K. Chen-Wiegart, J.J. Wang, H.H. Kung, J. Wang, S.A. Barnett, K.T. Faber, X-ray nanotomography analysis of the microstructural evolution of LiMn2O4 electrodes, J. Power Sources 360 (2017) 460–469.
[40] L.S. Li, Y.C.K. Chen-Wiegart, J.J. Wang, P. Gao, Q. Ding, Y.S. Yu, F. Wang, J. Cabana, J. Wang, S. Jin, Visualization of electrochemically driven solid-state phase transformations using operando hard X-ray spectro-imaging, Nat. Commun. 6 (2015).
[41] J. Wang, Y.-cK. Chen-Wiegart, J. Wang, In situ chemical mapping of a lithium-ion battery using full-field hard X-ray spectroscopic imaging, Chem. Commun. 49 (2013) 6480–6482.
[42] K. Sun, C.H. Zhao, C.H. Lin, E. Stavitski, G.J. Williams, J.M. Bai, E. Dooryhee, K. Attenkofer, J. Thieme, Y.C.K. Chen-Wiegart, H. Gan, Operando multi-modal synchrotron investigation for structural and chemical evolution of cupric sulfide (CuS) additive in Li-S battery, Sci. Rep. 7 (2017).
[43] F. Lin, Y.J. Liu, X.Q. Yu, L. Cheng, A. Singer, O.G. Shpyrko, H.L.L. Xing, N. Tamura, C.X. Tian, T.C. Weng, X.Q. Yang, Y.S. Meng, D. Nordlund, W.L. Yang, M.M. Doeff, Synchrotron X-ray analytical techniques for studying materials electrochemistry in rechargeable batteries, Chem. Rev. 117 (2017) 13123–13186.
[44] J. Nelson, S. Misra, Y. Yang, A. Jackson, Y.J. Liu, H.L. Wang, H.J. Dai, J.C. Andrews, Y. Cui, M.F. Toney, In Operando X-ray diffraction and transmission X-ray microscopy of lithium sulfur batteries, J. Am. Chem. Soc. 134 (2012) 6337–6343.
[45] C. Zhao, T. Wada, V. De Andrade, G.J. Williams, J. Gelb, L. Li, J. Thieme, H. Kato, Y.-C.K. Chen-Wiegart, Three-dimensional morphological and chemical evolution of nanoporous stainless steel by liquid metal dealloying, ACS Appl. Mater. Interfaces 9 (2017) 34172–34184.
[46] J. Nelson, S. Misra, Y. Yang, A. Jackson, Y. Liu, H. Wang, H. Dai, J.C. Andrews, Y. Cui, M.F. Toney, In Operando X-ray diffraction and transmission X-ray microscopy of lithium sulfur batteries, J. Am. Chem. Soc. 134 (2012) 6337–6343.
[47] P. Pietsch, M. Hess, W. Ludwig, J. Eller, V. Wood, Combining operando synchrotron X-ray tomographic microscopy and scanning X-ray diffraction to study lithium ion batteries, Sci. Rep. 6 (2016).
[48] P. Pietsch, D. Westhoff, J. Feinauer, J. Eller, F. Marone, M. Stampanoni, V. Schmidt, V. Wood, Quantifying microstructural dynamics and electrochemical activity of graphite and silicon-graphite lithium ion battery anodes, Nat. Commun. 7 (2016).
[49] V. De Andrade, A. Deriy, M.J. Wojcik, D. Gürsoy, D. Shu, K. Fezzaa, F. De Carlo, Nanoscale 3D imaging at the advanced photon source, SPIE Newsroom (2016), https://doi.org/10.1117/2.1201604.006461.
[50] K. Jefimovs, J. Vila-Comamala, M. Stampanoni, B. Kaulich, C. David, Beam-shaping condenser lenses for full-field transmission X-ray microscopy, J. Synchrotron Radiat. 15 (2008) 106–108.
[51] F. De Carlo, D. Gursoy, F. Marone, M. Rivers, D.Y. Parkinson, F. Khan, N. Schwarz, D.J. Vine, S. Vogt, S.C. Gleber, S. Narayanan, M. Newville, T. Lanzirotti, Y. Sun, Y.P. Hong, C. Jacobsen, Scientific data exchange: a schema for HDF5-based storage of raw and analyzed data, J. Synchrotron Radiat. 21 (2014) 1224–1230.
[52] D.M. Pelt, V. De Andrade, Improved tomographic reconstruction of large-scale real-world data by filter optimization, Adv. Struct. Chem. Imaging 2 (2017) (17-17).
[53] D.M. Pelt, D. Gursoy, W.J. Palenstijn, J. Sijbers, F. De Carlo, K.J. Batenburg, Integration of TomoPy and the ASTRA toolbox for advanced processing and reconstruction of tomographic synchrotron data, J. Synchrotron Radiat. 23 (2016) 842–849.
[54] E.X. Miqueles, J. Rinkel, F. O'Dowd, J.S.V. Bermudez, Generalized Titarenko's algorithm for ring artefacts reduction, J. Synchrotron Radiat. 21 (2014) 1333–1346.
[55] R. Kataoka, Y. Oda, R. Inoue, M. Kitta, T. Kiyobayashi, High-strength clad current collector for silicon-based negative electrode in lithium ion battery, J. Power Sources 301 (2016) 355–361.
[56] L.L. Luo, J.S. Wu, J.Y. Luo, J.X. Huang, V.P. Dravid, Dynamics of electrochemical lithiation/delithiation of graphene-encapsulated silicon nanoparticles studied by in-situ TEM, Sci. Rep. 4 (2014).
[57] M. Gu, Y. Li, X.L. Li, S.Y. Hu, X.W. Zhang, W. Xu, S. Thevuthasan, D.R. Baer, J.G. Zhang, J. Liu, C.M. Wang, In situ TEM study of lithiation behavior of silicon nanoparticles attached to and embedded in a carbon matrix, ACS Nano 6 (2012) 8439–8447.
[58] Y.C.K. Chen-Wiegart, T. Wada, N. Butakov, X.H. Xiao, F. De Carlo, H. Kato, J. Wang, D.C. Dunand, E. Maire, 3D morphological evolution of porous titanium by X-ray micro- and nano-tomography, J. Mater. Res. 28 (2013) 2444–2452.
[59] J.W. Choi, J. McDonough, S. Jeong, J.S. Yoo, C.K. Chan, Y. Cui, Stepwise nanopore evolution in one-dimensional nanostructures, Nano Lett. 10 (2010) 1409–1413.
[60] Q. Yuan, F. Zhao, Y. Zhao, Z. Liang, D. Yan, Reason analysis for Graphite-Si/SiOx/C composite anode cycle fading and cycle improvement with PI binder, J. Solid State Electrochem. 18 (2014) 2167–2174.
[61] D. Mazouzi, Z. Karkar, C.R. Hernandez, P.J. Manero, D. Guyomard, L. Roue, B. Lestriez, Critical roles of binders and formulation at multiscales of silicon-based composite electrodes, J. Power Sources 280 (2015) 533–549.
[62] Y. Oumellal, N. Delpuech, D. Mazouzi, N. Dupre, J. Gaubicher, P. Moreau, P. Soudan, B. Lestriez, D. Guyomard, The failure mechanism of nano-sized Si-based negative electrodes for lithium ion batteries, J. Mater. Chem. 21 (2011) 6201–6208.
[63] F. Tariq, V. Yufit, D.S. Eastwood, Y. Merla, M. Biton, B. Wu, Z. Chen, K. Freedman, G. Offer, E. Peled, P.D. Lee, D. Golodnitsky, N. Brandon, In-operando X-ray tomography study of lithiation induced delamination of Si based anodes for lithium-ion batteries, ECS Electrochem. Lett. 3 (2014) A76–A78.
[64] I. Choi, M.J. Lee, S.M. Oh, J.J. Kim, Fading mechanisms of carbon-coated and disproportionated Si/SiOx negative electrode (Si/SiOx/C) in Li-ion secondary batteries: dynamics and component analysis by TEM, Electrochim. Acta 85 (2012) 369–376.

Chonghang Zhao is currently pursuing his Ph.D. in the Department of Materials Science and Chemical Engineering, at Stony Brook University. Previously he obtained his B.S. degree from Tianjin University. His research interests focus on fabricating nanoporous materials for energy applications, in situ characterization on energy related applications, as well as 3D tomography characterization and analysis.

Takeshi Wada is an Associate professor of Institute for Materials Research (IMR), and Graduate School of Engineering of Tohoku University. His research interests focus on metallic glass, amorphous alloy and porous metal. Based on the strategy of alloy design for metallic glass formation, he and his group developed new dealloying methods for fabricating nanoporous metals and study their fundamental mechanisms and applications.

Vincent De Andrade is beamline scientist at the Advanced Photon Source at Argonne National Laboratory where he is leading the scientific program of a Transmission X-ray Microscope, an instrument dedicated to in-situ X-ray nanotomography. His research focuses on instrumentation development for imaging techniques applied to Materials and Environmental Science. After the obtaining of a Ph.D. degree in Earth Science, he served in the synchrotron community for more than 10 years, at the ESRF first, then at NSLS-II where he co-designed one of the first project beamlines before joining the imaging group at APS in 2014.

Doga Gursoy is an assistant computational scientist at the X-ray Science Division of Advanced Photon Source. His research focus has been primarily on the modeling and algorithmic aspects of computational imaging and inverse problems with specific applications in biomedical and materials sciences. He has a broad interest in modeling of forward and inverse photon transport processes and numerical methods for solving large-scale parameter estimation problems.

Hidemi Kato is a Professor of Institute for Materials Research (IMR), and Graduate School of Biomedical Engineering, Tohoku University. His research interests focus on wide field topics on metallic glass including relaxation/viscous flow and structural characteristics, and recently, synthesis and their application (battery, capacitor, catalyst) of nano- and submicron- porous metals by the original method of his group, liquid metal dealloying.

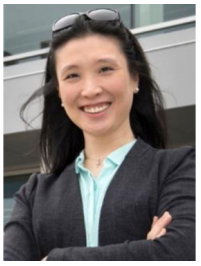

Y.-c. Karen Chen-Wiegart is currently an Assistant Professor in the Department of Materials Science and Chemical Engineering at Stony Brook University (SBU). She also holds a Joint Appointment at the National Synchrotron Light Source – II, Brookhaven National Laboratory (BNL). Her group emphasizes on understanding the kinetics and dynamics behavior of materials by studying their morphological, chemical and structural evolution, particular ly utilizing advanced synchrotron methods. She obtained her Ph.D. from Northwestern University and B.S. from National Taiwan University. She received NSF CAREER Award in 2018 and is part of two Energy Frontier Research Centers.